UC San Diego
UC San Diego Previously Published Works

Title

Computer image modeling of pentamer packing in polyoma virus "hexamer" tubes

Permalink

https://escholarship.org/uc/item/6mm8h66b

Journal

Ultramicroscopy, 13(1-2)

ISSN

0304-3991

Authors

Baker, TS
Caspar, DLD

Publication Date

1984

DOI

10.1016/0304-3991(84)90064-0

Peer reviewed

COMPUTER IMAGE MODELING OF PENTAMER PACKING IN POLYOMA VIRUS "HEXAMER" TUBES

T.S. BAKER * and D.L.D. CASPAR

Rosenstiel Basic Medical Sciences Research Center, Brandeis University, Waltham, Massachusetts 02254, USA

Polymorphic assemblies of polyoma virus capsomeres that have been called "hexamer" tubes (because the morphological units are six-coordinated) are, in fact, built of pentamers, as is the icosahedrally symmetric T = 7d virus capsid. We have established the pentameric form of the capsomeres in the "hexamer" tubes by analysis of low-irradiation micrographs. Methods for generating computer image models with adjustable parameters have been developed to fit micrographs of negatively stained, flattened tubes. The image model has been refined to define the packing arrangement and substructure of the pentametric capsomeres in the superimposed top and bottom layers of the tube and to represent the differential flattening, lateral distortion and staining of the two sides. Information about the structure that is not directly accessible by conventional image filtering methods can be obtained by image modeling methods.

1. Introduction

Model building has been used to resolve critical aspects of papova virus particle structure. Klug and Finch [1,2] used shadowgraphs from Geodestix models to simulate images of negatively stained human wart and rabbit papilloma viruses and settle the controversy concerning the distribution and number of morphological units in the virus shell [3–5]. This study helped explain how one-sided images arise when stain is unevenly distributed on the top and bottom surfaces of the specimen attached to the support film: virus particles often stain equally on the two surfaces, resulting in images which can be difficult to interpret due to superposition effects. Images corresponding to variable staining on the two sides were simulated with an analogue model [6].

Images of uniformly stained particles were accurately represented by generating models with adjustable parameters in a computer [7]. The excellent correspondence between stereo micrographs and models rotated through equivalent viewing orientations showed that negative stains can preserve icosahedral symmetry and faithfully outline structural features to at least 2nm resolution. This pioneering work by Klug and Finch [7] presented a convincing demonstration of the power of computer modeling.

Kiselev and Klug [8] modeled two-sided unfiltered and one-sided optically filtered images of one of the major classes of human wart and rabbit papilloma tube aggregates. This model simulation produced compelling evidence for the existence of a polymorphic aggregate built of pentameric capsomeres arranged in a novel type of pentagonal tessellation.

The recent discovery that all 72 capsomeres in polyoma virus capsids are pentameric [9] was based on refinement of models representing the coarse surface features revealed by electron microscopy [10] against X-ray diffraction data. This result contradicted the presumption that the T = 7 icosahedral papova virus capsids should be built of 12 pentameric and 60 hexameric capsomeres arranged to preserve quasi-equivalent bonding [11]. To further explore this problem we reexamined the "hexamer" class of tubes [12], studied by Kiselev and Klug [8,13], which were presumed to contain

---

* Present address: Department of Biological Sciences, Purdue University, West Lafayette, Indiana 47907, USA.
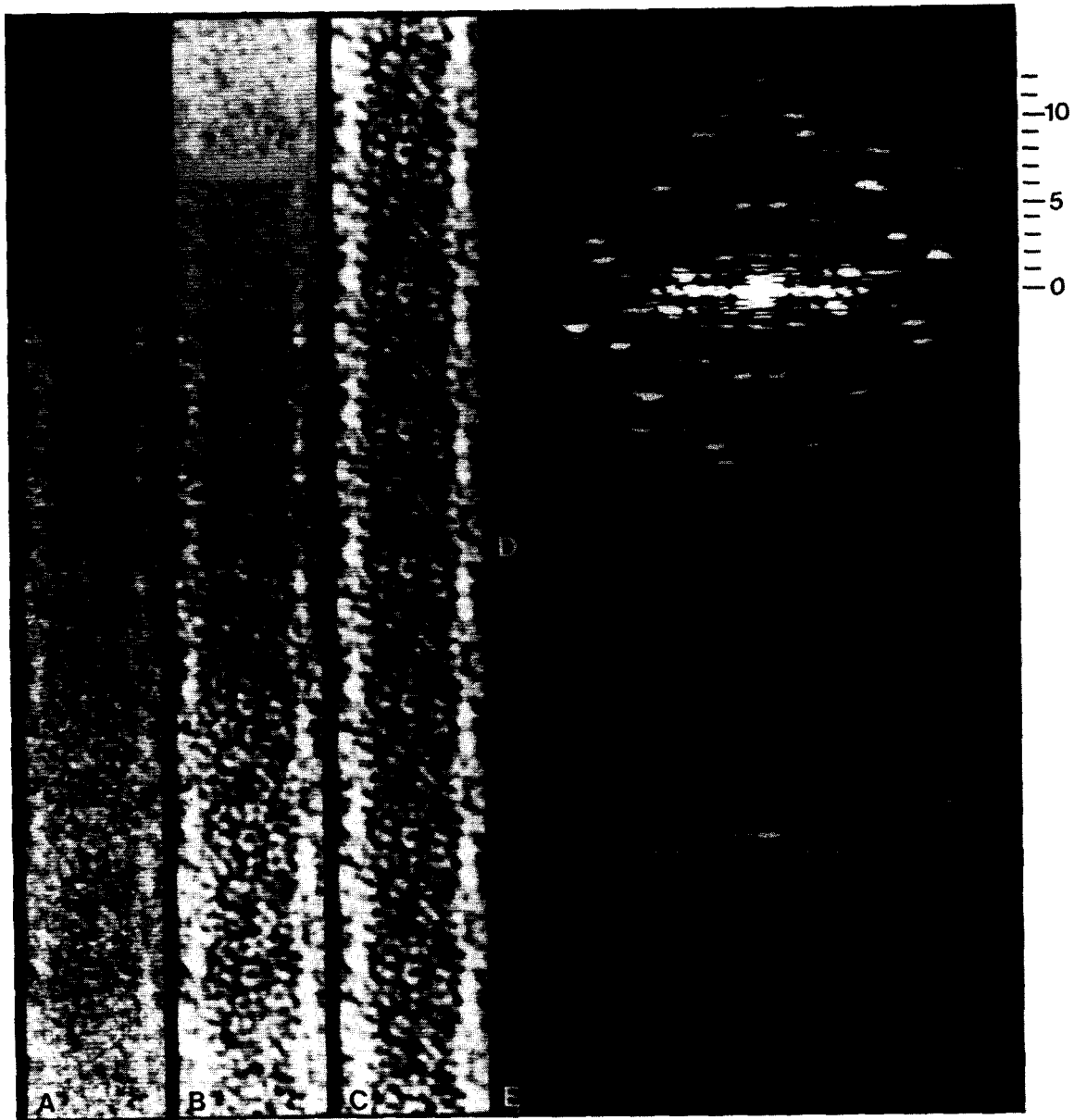
Fig. 1. (A) Unfiltered, digitized image of a typical negatively stained polyoma "hexamer" tube. There are six axial repeats of the helical structure included in the boxed area. The prominent near-axial helical lines on the near (away from grid) and far sides of the tube, corresponding to the packing of capsomeres in rows close to the axial direction, are easier to see when the image is viewed at a glancing angle close to the axial direction.

(B) "Locally" averaged tube image produced by Fourier-inverting the weighted diffraction pattern of (A), as described in the text. The procedure produces a result equivalent to that obtained by direct photographic translational superposition of (A), where shorter exposures are given for successive superpositions.

(C) Long-range average image, produced as described in (B), but where all axial repeats in (A) are averaged with nearly identical weight.

(D) Computed Fourier transform of (A). The positions of 13 layer lines in the top half are marked at the right. The strong peaks on the first non-equatorial layer line arise from the prominent near-axial helical lattice lines observed in the images (A)–(C).

(E) Filtered diffraction pattern, produced by truncating Fourier transform data away from the calculated layer line positions with a Gaussian weighting function (with scale length $\omega = 0.5$; see text), corresponding to the averaged image in (C). ω can be adjusted to control the extent of averaging ($\omega = 2.0$ for (B) and 0.5 for (C)).

hexameric capsomeres packed hexagonally in the cylindrical lattice of the tube. A new indexing of the reciprocal helical lattice was proposed which led to a computer-filtered image demonstrating that the repeating unit of the "hexamer" tubes consists of a pair of capsomeres. The capsomere packing arrangement in the "hexamer" tube surface lattice is closely related to the pentagonal tessellation previously described for the "pentamer" tubes [8,13].

Detailed modeling studies provide sensitive measures of the capsomere morphology and orientation, and have helped characterize the effects of differential staining and flattening of specimens prepared for microscopy. This report describes how model-fitting procedures have been used to analyze a typical "hexamer" tube of polyoma virus. Our aim is to investigate and compare the packing of pentameric morphological units in hexavalent environments in both mature virions and in tubes. The modeling studies also suggest a new way to filter two-sided images when diffraction from the opposite halves interfere with each other and cannot be separated with conventional masking procedures [14,15].

2. Experimental

Specimen: Fractions enriched in tube aggregates were prepared by W.T. Murakami (Brandeis University).

Electron microscopy: 0.1 mg/ml samples were adsorbed to carbon or carbon-Formvar support films, stained with 1% aqueous, unbuffered uranyl acetate and images recorded at 41,000 magnification in a Philips EM301 electron microscope using minimal irradiation conditions (1000–2000 e$^-$/nm^2 see ref. [16]). The image analyzed in detail (fig. 1A) is the same one described previously [12] and is typical of the major class of "hexamer" tube. It was selected from other similar images on the basis of the quality of its optical diffraction pattern and because there are several aligned axial repeats within the same particle.

Image processing: The micrograph was digitized on an Optronics P1000 Photoscan rotating drum scanning microdensitometer (Optronics Interna-

tional, Inc., Chelmsford, MA) using a 25 μm step raster (equivalent to 0.61 nm sampling at the specimen) and displayed on a TV graphics monitor (either a black and white Grinnell GMR-27, Grinnell Systems Corp., Santa Clara, CA; or a color AED512, Advanced Electronics Design, Inc., Sunnyvale, CA). Intensities in the image that are well outside the normal range, due to obvious flaws such as dust specks or scratches on the micrograph, were rescaled by replacing the abnormal intensity values with the mean of the remaining image intensities. This procedure reduces the noise contributed by such flaws in averaged images. An appropriate area was boxed, floated and its Fourier transform computed on a VAX 780 minicomputer (Digital Equipment Corp., Maynard, MA). Grey level (256 or fewer steps) displays of observed and calculated images, diffraction patterns and line plots were photographed on Panatomic-X or LPD-4 film (Eastman Kodak Co. Rochester, NY) using a Matrix Model 3000 Color Graphic Recorder (Matrix Instruments Inc., Northvale, NJ).

3. Image alignment and scaling

The image was rotated and reinterpolated so that layer lines would be exactly sampled in the discrete Fourier transform [17]. The orientation and spacing of layer lines was determined by projecting the amplitudes in the diffraction pattern onto meridian lines within a small angular range of the vertical transform sampling direction (fig. 2). The line which gives maximum reinforcement of the projected layer line data defines the angle by which the image must be rotated to adjust the horizontal sampling direction in the transform to be parallel with the layer lines. Fourier transforms of the projected amplitude data (corresponding to central lines through the autocorrelation function of the image) provide an additional measure of the alignment and also provide an accurate measure of the layer line spacing (fig. 2). The Fourier transform of the line of projected amplitude data from the best orientation will have a prominent peak at a distance from the origin reciprocally related to the layer line spacing. The amplitude of the peak is
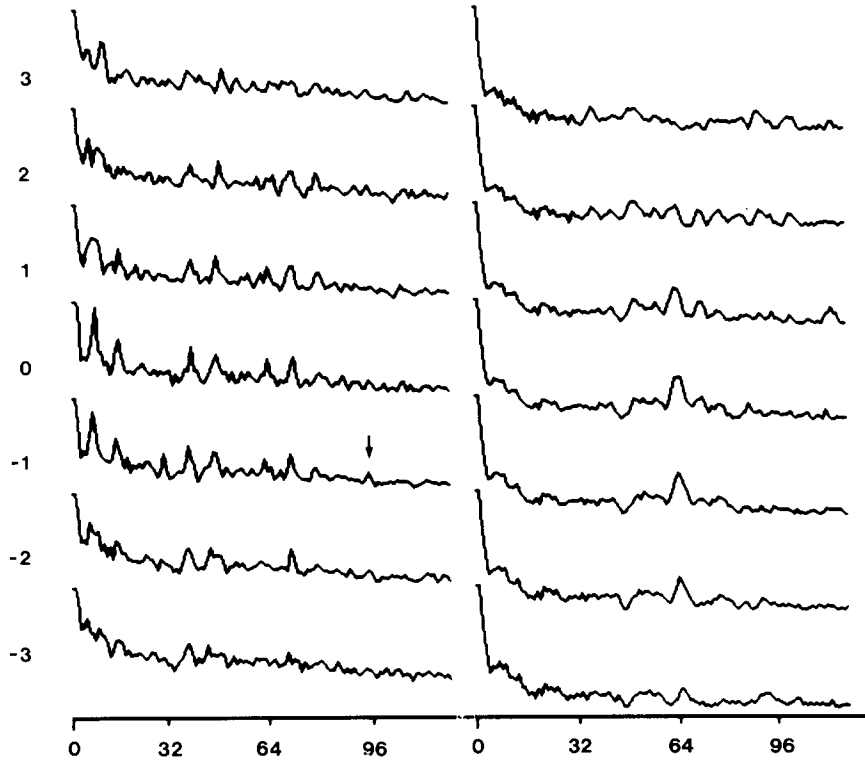
Fig. 2. Determination of image orientation and layer line spacing. Left column: Projections of the diffraction pattern amplitudes (fig. 1D) onto lines within 3° of the vertical sampling direction in the computed Fourier transform. Right column: Fourier transforms of each line of projected amplitude data at the left. Maximum reinforcement of the layer lines occurs on the projected line between 0° and −1° from the vertical (negative sign corresponds to a counterclockwise rotation of the line away from the vertical sampling direction of the digitized image). The line at −1° rotation angle shows maximum reinforcement of the 12th layer line (marked by arrow). The Fourier transform of this projected data shows a single, prominent peak 64 units from the origin, arising from exact sampling of the layer lines every eighth (= 512/64) point of the projected data.
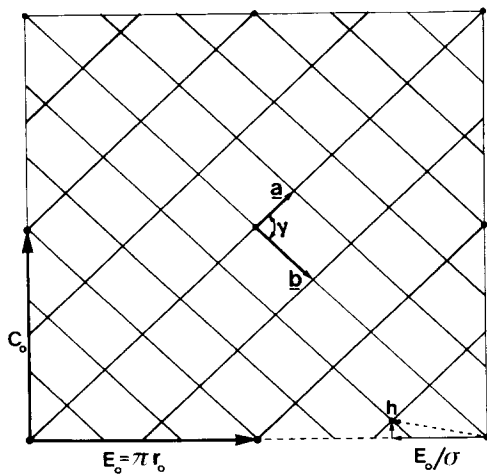

Fig. 3. Surface lattice of the polyoma virus hexamer tube (shown in fig. 1A). This diagram corresponds to two axial repeats of the helix net cut along a line parallel to the axis (the

vertical direction) opened out flat and viewed from the outside. The lattice with unit vectors a, b and included angle γ has plane group symmetry p2 and the origin is at one of the 2-fold axes. (The unit cell shown is the most nearly orthogonal but other, more oblique, cells could also be chosen to represent the lattice symmetry.) The equatorial vector E_0, connecting nearest equivalent points in the equatorial plane, corresponds to a rotation of 180° about the helix axis since the tube has a parallel 2-fold symmetry axis. The particular relation observed between the axial repeat vector C_0 and the equatorial vector E_0 requires that $|b| = 1.5 \; |a|$ and $\tan \gamma/2 = C_0/E_0$. The basic helical symmetry, corresponding to the smallest axial translation plus rotation relating equivalent points, is represented by the dotted arrow at the lower right that is directed in the $\overline{1}, \overline{1}$ direction of the plane lattice. The unit axial translation $h = C_0/12$ and the screw symmetry $\sigma = -12/5 = -2.4$ corresponding to a left-handed rotation of $\pi/\sigma = 75°$. The line group symmetry for this helical lattice is designated $D_2 S_{\overline{2.4}}$.

directly related to the extent of layer line rein-
forcement in the projected data. Since the layer
line spacing need not be an integral number, the
image size was rescaled by interpolation so that
the layer lines were equally sampled in the Fourier
transform.

4. Helical surface lattice

Determination of the helical lattice symmetry
did not follow directly from examination of the
images or their diffraction patterns [12]. Model
simulations of the two-sided images unequivocally
established the correct helical symmetry since
models built with incorrect symmetry did not
simulate the observed superposition patterns. The
problems with determining the helical symmetry
from inspection of the image data can best be
assesed following the description of the surface
lattice.

The surface lattice of the "hexamer" tube
selected for detailed analysis is diagrammed in fig.
3. A number of tubes with the same symmetry
were identified: other tubes have larger or smaller
diameters but similar orientation of the surface
lattice unit cell relative to the tube axis. The
surface lattice has p2 plane group symmetry, and
one of the four classes of 2-fold axis of this plane
group is chosen as origin. The other 2-fold axes are
at the midpoints of the a and b axes and at the
middle of the cell. The tube surface lattice is
uniquely specified by the length of the vectors a
and b of the p2 unit cell, the angle γ between
them, and the indices of the circumferential vector,
corresponding to the base of the lattice in fig. 3.
This circumferential vector is $V = 6a + 4b$. Since
the indices have the common factor 2, this tube
has a parallel 2-fold axis, and the vector between
nearest equivalent points in the equatorial direc-
tion, $E_0 = 3a + 2b$, corresponds to a 180° rotation
about the tube axis.

The axial repeat vector is $C_0 = 3a - 2b$. Since
$C_0 \times E_0 = 0$, $|b| = 1.5|a|$. This simple relation be-
tween a and b, which is a consequence of the
relation between the axial and equatorial vectors,
is not a general property of all "hexamer" tube
surface lattices. In this particular case $|C_0| =$
$4b|\sin \gamma/2$ ($= 6a \sin \gamma/2$) and $|E_0| = 4b \cos \gamma/2$,

since the equatorial vector bisects the angle γ.

The length of the axial repeat is $C_0 = 40.7$ nm.
This distance is measured with a precision of
about 1% by averaging over six repeats. When the
tube is dried on the grid, it flattens and the near
side (away from the grid) shrinks relative to the far
side. The surface lattice unit cell parameters can-
not be measured with the same precision as the
axial repeat, but the ratio of b to a does not
change since the differential shrinkage only occurs
in the lateral direction. Thus, the length and direc-
tion of the axial vector are the same for the near
and far sides. The best measurement of unit cell
parameters (by fitting a reciprocal lattice net to
the diffraction pattern of fig. 1D) is for the far side
$a = 9.89$ nm, $b = 14.84$ nm, $\gamma = 86.6°$; and for the
near side $a = 9.15$ nm, $b = 13.73$ nm, $\gamma = 95.7°$.
The decrease for the near side corresponds to a
lateral shrinkage of about 14%.

The tube surface lattice can also be uniquely
specified by its line group symmetry and screw
axis translation. Line group symmetries are desig-
nated $C_n S_\sigma$ or $D_n S_\sigma$, where C_n and D_n represent the
cyclic or dihedral n-fold rotational point group
symmetry and S_σ represents the σ-fold screw sym-
metry. The screw operation consists of a transla-
tion by a distance h parallel to the axis coupled
with a rotation ϕ, to the right or left, about this
axis. The order of the screw symmetry is defined
as $\sigma = 2\pi/n\phi$ where n is the order of the rota-
tional symmetry. The polyoma tubes have dihedral
symmetry since the p2 surface lattice generates
dyads perpendicular to the tube axis. The tube in
fig. 1A has a parallel 2-fold axis, thus the point
group symmetry is D_2. Along the basic helical
path, the unit axial translation is $h = C_0/12 = 3.39$
nm and the rotation is $\phi = -5\pi/12 = -75°$ (with
a negative sign for the left-handed twist). Thus,
$\sigma = -12/5 = -2.4$ and the line group symmetry
is $D_2 S_{\overline{2.4}}$.

The screw symmetry can be any real number,
thus there is some finite experimental uncertainty
in its measurement. For the tube in fig. 1A the
vector $3a - 2b$ is within $\pm 0.5°$ of the tube axis.
This corresponds to an uncertainty of about 0.2%
in the value of $\sigma = -2.40$. The linear distance in
the tube surface covered by the $-75°$ rotation is
determined by the radius of the tube. The dimen-

sions of the far surface of the flattened tube correspond to a radius $r_0 = 13.75$ nm, which would be the radius of strongest lateral contact between capsomeres if there is no distortion on flattening. The uncertainty in the estimate of the radius of the unflattened tube is large, but its helical symmetry is determined with high precision from the image modeling.

The problems involved in estimating the radius of the helical lattice from the image of the flattened tube are related to the difficulties in determining the helical symmetry from measurements on the image or its diffraction pattern. In the surface lattice shown in fig. 3, there are 10 parallel helical paths connecting lattice points in the $1,\bar{1}$ direction corresponding to the near axial rows of capsomeres seen in fig. 1. If the tube were completely flattened, 5 such rows should be counted on each side. Since the degree of flattening cannot be directly assessed (cf. models in fig. 8), the number of near axial rows of capsomeres seen could correspond to from 9 to 12 helical paths.

The number of helical paths in any direction is determined by the index of the circumferential vector (cf. fig. 3). Measurements of the image or its diffraction pattern for helices such as the polyoma tubes, in which the circumference is large compared to the unit cell dimensions, may not uniquely define the indices of the circumferential vector. Small errors in measurement of the unit cell dimensions and orientation could lead to an incorrect estimate of which lattice vector is exactly perpendicular to the tube axis. For example, for the surface lattice in fig. 3, the angle between the circumferential vector ($6a + 4b$) and the vector with indices $7a + 5b$ is less than $2°$. If the 7,5 vector were, in fact, the circumferential vector, then it would be perpendicular to the axial $3,\bar{2}$ vector, and the ratio of the b to a unit cell axes would be decreased by about 1.5% and the circumference would increase by 21% compared to the lattice in fig. 3. The change in circumference is large, but it is within the range of variation in tube diameter due to the plausible differences in flattening illustrated in fig. 8; the small differences in unit cell axial ratio and orientation for these alternative surface lattices would be very difficult to distinguish experimentally.

The helical surface lattices with a $3,\bar{2}$ axial vector and either 6,4 or 7,5 circumferential vector would have similar surface appearances and diffraction patterns, but the descriptions of their helical symmetry are different. In the line group designation $D_n S_\sigma$, for the 6,4 circumferential vector, $n = 2$, $\sigma = -12/5$ and $h = C_0/12$: while for the 7,5 circumferential vector, $n = 1$, $\sigma = +29/12$ and $h = C_0/29$. These helices with 10 or 12 near axial rows of capsomeres can, however, be distinguished by the appearance of the superposition of near and far sides of the negatively stained tubes. Distinctive features in these superposition patterns are determined by the capsomere packing arrangement, independent of details in their substructure. Since the capsomere packing is evident from the filtered image [12], calculation of superposition patterns from low-resolution models of the approximately hexagonally packed capsomeres has provided a critical test to uniquely determine the helical symmetry of the tube. The superposition patterns are very sensitive to the azimuthal direction of view (cf. fig. 5) as well as to the index of the circumferential vector. A small gallery of different views of different helical models based on the same basic surface lattice is sufficient to identify both the symmetry and azimuthal orientation of any tube stained on both sides.

5. Image averaging and noise filtering

The image was averaged to improve the signal-to-noise ratio and facilitate comparisons with computed models. Since the axial repeat of the tube image is well determined, the image may be translationally averaged along the axial direction to give a clearer image of the superimposed near and far sides of the tube. The tube image was averaged using two similar procedures which multiply the observed Fourier transform with functions that suppress data away from the layer lines. The first method weights each point in the Fourier transform by

$$\exp\left[-(d/\omega)^2/2 \right],$$

where d is the distance of the transform point to the nearest layer line (in units of scan lines, with an 8-scan line separation between layer lines) and

ω is an adjustable scale length controlling the extent of averaging and noise reduction. The averaged image is computed from the inverse Fourier transform of the modified diffraction pattern. Each axial repeat in the locally averaged image arises from a weighted sum of neighboring repeats from the original image; repeats in the original image are averaged with their neighbors in a way that emphasizes the contribution of closer neighbors relative to those further away. This explains why the repeating units are less prominent at the top of the averaged image (fig. 1B; $\omega = 2.0$).

Averages where the axial repeats are all identical were produced either by reducing ω (fig. 1C; $\omega = 0.5$) or by zeroing the Fourier transform everywhere but directly on the sampled layer lines (fig. 11A). For the tube analyzed here, the layer lines occur on every eighth line of the discrete Fourier transform. When $\omega = 0.5$ the range of averaging extends over an axial distance of about eight repeats (fig. 1C), which is nearly equivalent to giving each repeat in real space equal weight since there are only six repeats in the portion of the image being averaged. In fig. 11A, all six repeats in the image have been averaged with equal weight corresponding to $\omega \approx 0$ which makes the reciprocal space weighting function a delta function. Since six repeats have been averaged, noise is reduced by $5/6$; additional noise was removed by imposing a 2.5 nm resolution cutoff before the diffraction data were inverse-Fourier-transformed to obtain the averaged image.

6. Computer modeling

Our analysis of the "hexamer" tubes indicated that they are composed of paired pentamers arranged so that the pentameric capsomeres are packed approximately hexagonally. The motif (pair of capsomeres) was modeled using four adjustable parameters as illustrated in fig. 4. Each capsomere consists of five Gaussian spheres of radii r_3 at a distance r_2 from a strict five-fold rotational symmetry axis. The pair of pentamers were oriented with a pair of edges apposed corresponding to the edge-to-edge contact seen in the capsid [9] and in the pentamer tubes [8]. The center-to-center sep-

aration of capsomeres in each pair is r_1 and the angular orientation of the pair relative to the direction of the tube axis is given by ψ. The pentamer pairs were arranged on a p2 plane surface lattice whose dimensions were measured from the indexed lattice of the experimental diffraction pattern corresponding to the far side of the tube facing the support film of the microscope grid. The surface lattice was rolled into a cylinder forming a
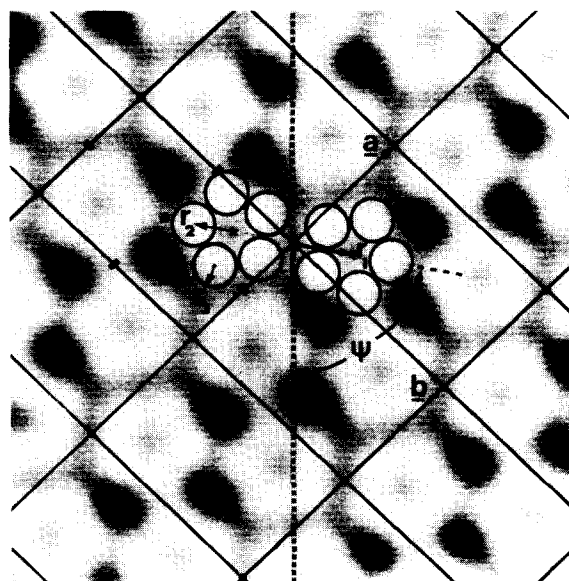

Fig. 4. Adjustable parameters of the paired pentamer model that were refined to fit the electron microscope image. The dimer of pentamers is constrained to have the line connecting their centers bisect the parallel pair of pentagon edges adjoining the 2-fold axis chosen as origin. The other classes of 2-fold axes, at the mid-point of the edges and at the center of the cell, are marked for one unit cell. The adjustable parameters are r_3, the radius of a subunit; r_2, the distance of the subunit center from the center of the pentagon; r_1, the distance of the pentagon center from the 2-fold axis; and ψ, the angle between the vector r_1 and the line parallel to the axis through the 2-fold axis. The unit vectors **a** and **b** are drawn with the dimensions of the tube surface lattice in contact with the grid (the far side), which appears to be the least distorted laterally. The radius of the tube corresponding to this surface is $r_0 = 13.75$ nm. The parameters which best fit the experimental image are $\psi = 80°$, $r_1 = 4.25$ nm, $r_2 = 2.72$ nm and $r_3 = 1.75$ nm. With these parameters, the edge-to-edge contacts in the nearly horizontal and vertical directions are quasi-equivalently related by the local 5-fold axes of the capsomeres. This quasi-symmetry relation was not imposed on the model, but is implied by the image data.

helical lattice with the appropriate diameter ($2r_0$) and axial repeat C_0. The three-dimensional model density distribution was projected along a chosen azimuthal orientation (η) to give the two-dimensional superposition image which was subsequently Fourier-transformed and compared with the experimental data. The superimposed image of the near and far sides of the tube changes significantly for very small changes in the azimuthal orientation angle η (fig. 5).

The parameters r_1, r_2, r_3, ψ and η were initially estimated by direct inspection of the averaged image (fig. 1C) which shows a distinctive pentago-

nal "eye" feature near the axis arising from almost exact superposition of capsomeres on the two sides of the stained specimen. The effect of variation in orientation of the pair of pentamers in the unit cell, defined by the angle ψ, is illustrated in fig. 6; and coupled variation in the size and separation of the pentamers, defined by r_1, r_2 and r_3, is illustrated in fig. 7.

Differential flattening and staining. Both the experimental image (fig. 1A) and its diffraction pattern (fig. 1D) show clear departures from the mirror symmetry that would be expected if the helical structure with a parallel 2-fold axis were
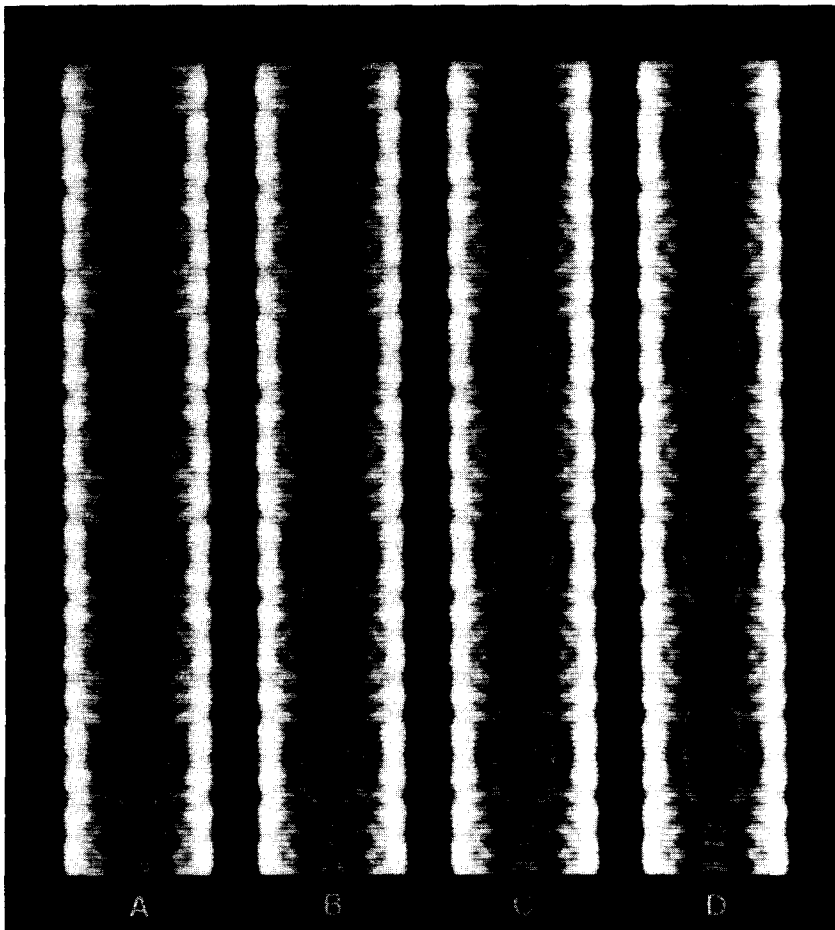
Fig. 5. Views of a helically symmetric model computed with equal contrast on the near and far sides and without flattening. The model is rotated by 1.25° about its axis between successive images, starting with the orientation in (A) which best represents the orientation of the tube in fig. 1. The range within which views are unique is 3.75° ($2\pi/96$) for a helical structure with the surface lattice symmetry shown in fig. 3. (Other model parameters are the same as in fig. 4.)
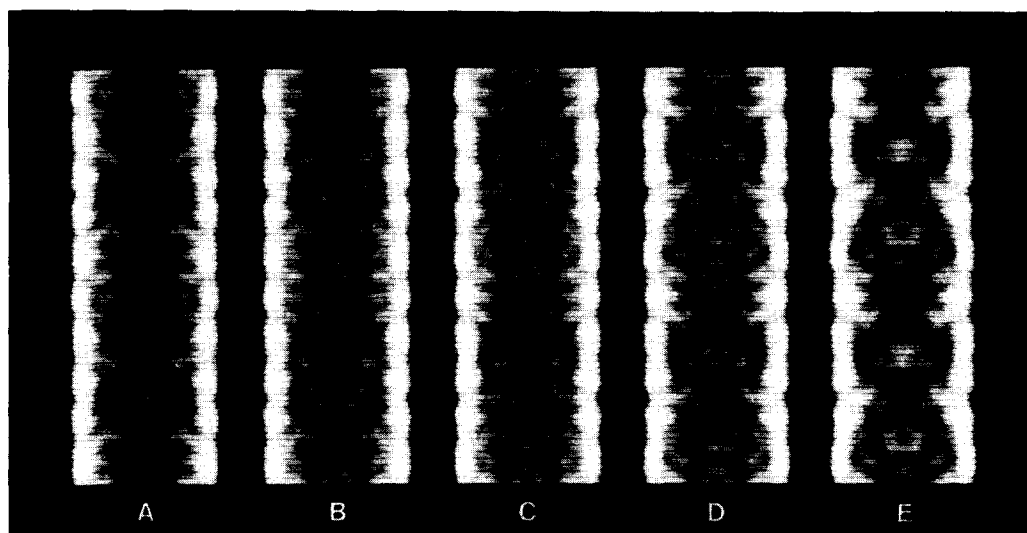
Fig. 6. Helically symmetric models with variation in the angular orientation of the motif. ($\psi = 70°$, $75°$, $80°$, $85°$ and $90°$ for (A)–(E); other parameters are the same as in fig. 4.)

undistorted. Loss of mirror symmetry (across the tube axis of the image or the vertical line of the diffraction pattern) is mainly attributed to the effects of differential flattening and staining of the two halves of the specimen prepared for electron microscopy. Several schemes for modeling the specimen flattening were tested. The effects of symmetric and asymmetric flattening are illustrated in figs. 8 and 9, respectively. An asymmetrically flattened model gives good agreement with the observed images. Elliptically distorted models could not be adjusted to approximate the
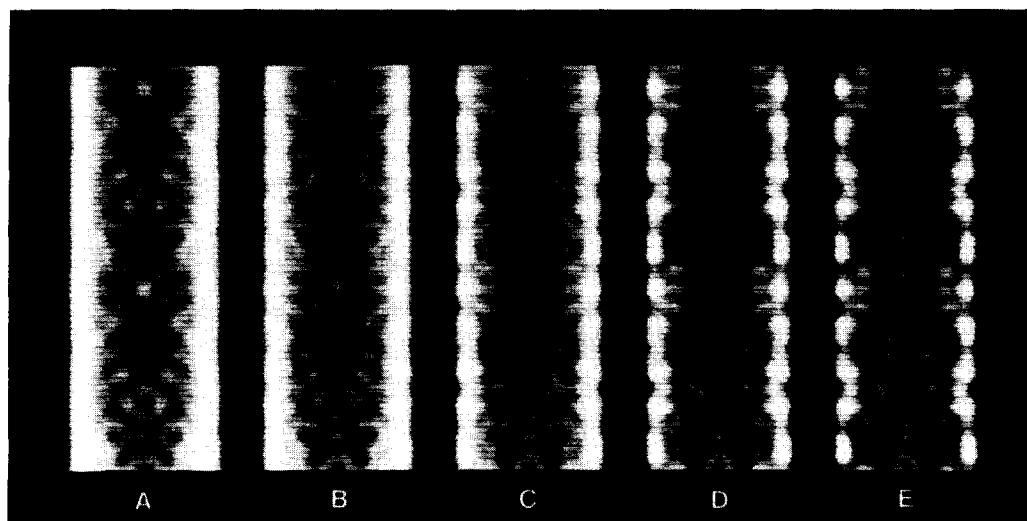
Fig. 7. Helically symmetric models with variation in the motif size. (r_1, r_2 and r_3 are all scaled by 1.11, 1.06, 1.00, 0.94 and 0.89 relative to the values given in fig. 4 for models A-3.)

experimental data. Difference in stain contrast on the two sides was modeled (fig. 10) by varying the mass density of the capsomere subunits on the near and far sides.

Comparison and refinement of models with experimental data. Parameters such as the axial repeat distance and the helical surface lattice symmetry are fixed for the particular tube image analyzed. Other parameters in the model were adjusted by an iterative trial-and-error procedure until a reasonable fit with the experimental data was obtained. Judgement of fit was based on comparing both the experimental and model

images and their diffraction patterns. Fig. 11 compares the axially averaged image (A) with a refined model (B) and fig. 12 compares the corresponding computed diffraction patterns. Fig. 13 compares the experimental and model diffraction data along 12 non-equatorial layer lines.

The refinement procedure was aided by the fact that certain layer lines are more sensitive than others to adjustments of particular parameters. For example, on layer line 2 (fig. 13) the outer peaks are sensitive to differences in contrast between the near and far sides whereas the two peaks near the meridian are more affected by the orien-
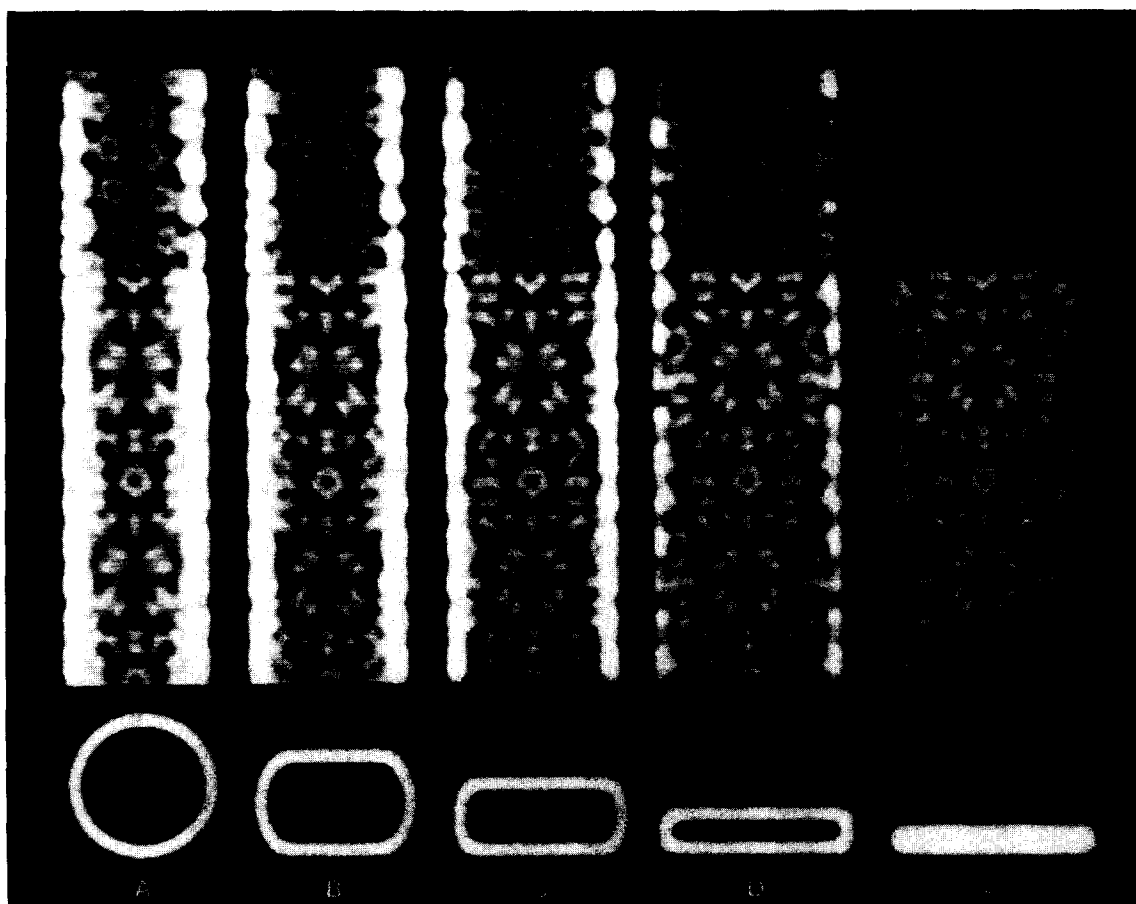

Fig. 8. Symmetrically flattened models with variation in the extent of flattening on the two sides. The upper third of each view shows only the near half. End-on views along the axis are shown below each corresponding view normal to the flattened surface. The fraction of each model which is flattened is 0.00, 0.50, 0.67, 0.83 and 1.00 for (A)–(E). The widths of the models (relative to an unflattened model) are 1.00, 1.08, 1.18, 1.34 and 1.57 ($= \pi/2$) for (A)–(E). (Other model parameters are the same as for fig. 4.)
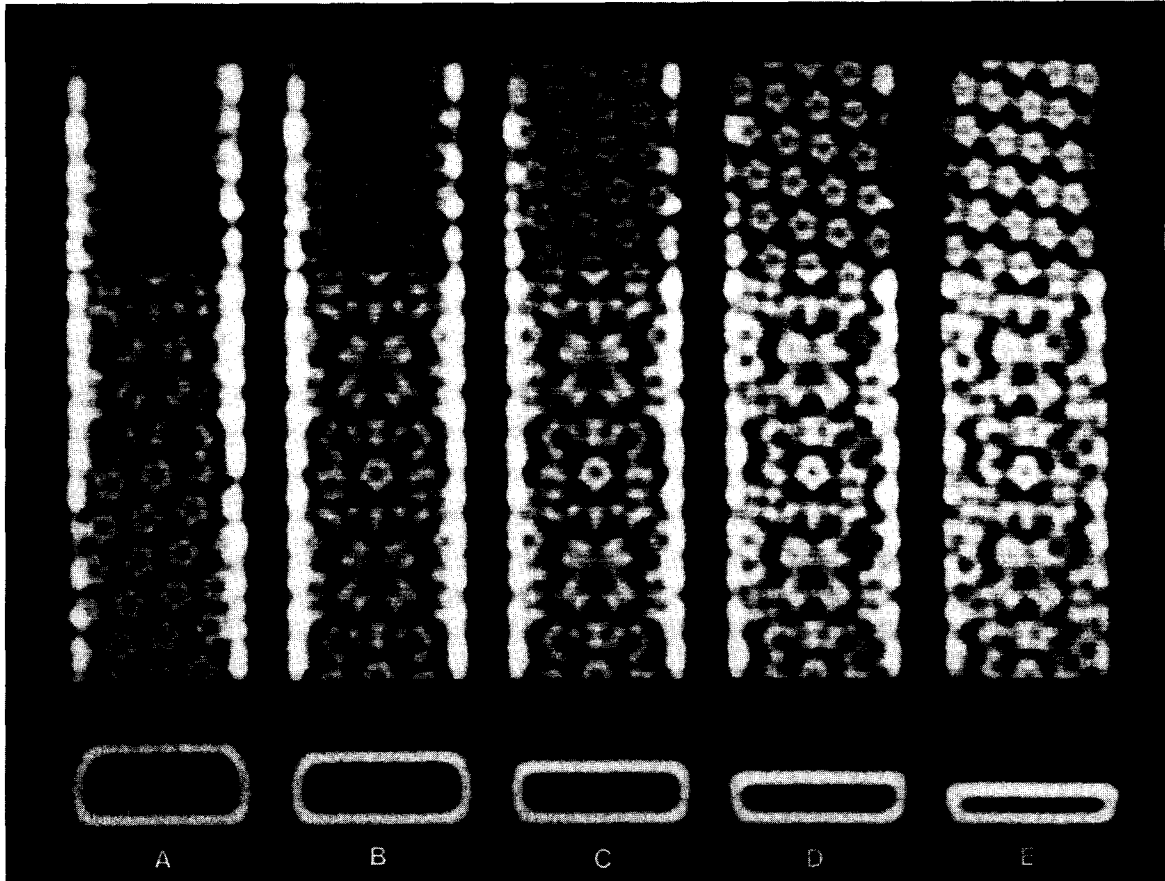
Fig. 9. Asymmetrically flattened models with variable flattening and lateral distortion of the surface lattice on the near side. In all models the far half is flattened to the same extent (0.72), thus fixing the width at 1.23 times that of an unflattened model. Motifs in the near half are expanded (A, B) or compressed (C, D, E) in a direction normal to the tube axis in the plane of flattening, to maintain the particle width and accommodate flattening which differs from that on the far side. The flattened portion of the near side is laterally distorted relative to the flattened portion of the far side by 1.14, 1.04, 0.96, 0.87 and 0.78 for (A)-(E). The upper third of each side view shows the near side only. The far side (same for all models) is shown in the lower third of the model A. Cross-sectional views of the five models appear below each corresponding projected view normal to the surface. (Other parameters are the same as for fig. 4.)
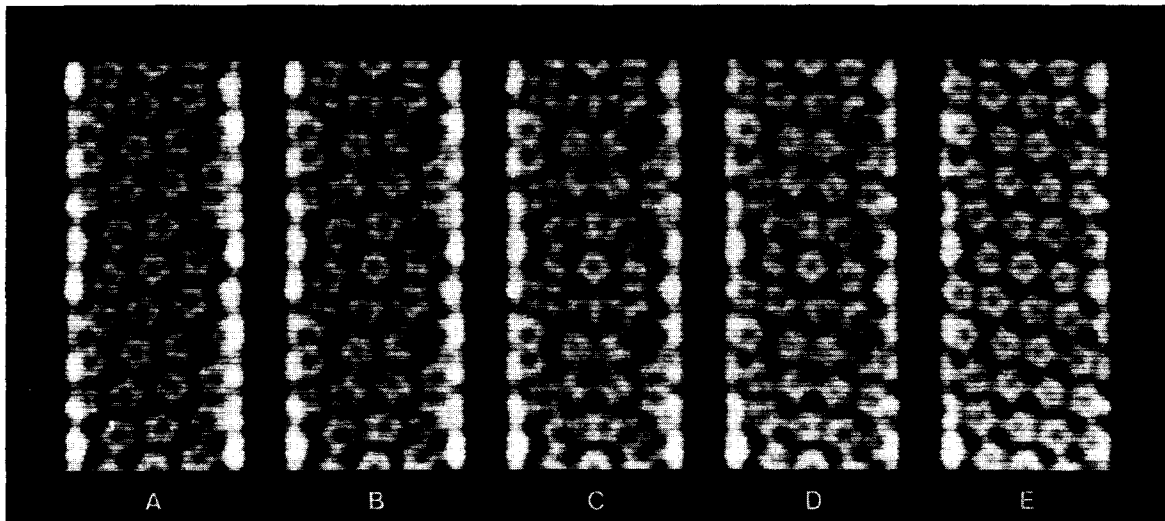

Fig. 10. Models computed with differential contrast on the near and far halves. The relative contrasts between near and far sides for (A)-(E) are 4.0, 2.0, 1.0, 0.5 and 0.25. (Other model parameters are the same as for fig. 9D.)

tation of the motif; the position and shape of the main peaks on layer line 3 are sensitive to the degree of differential flattening in the two sides.

Although individual parameters may be refined independently from all others, some such as r_1, r_2 and r_3 are strongly coupled. It is reasonable, for instance, to expect r_1 and r_2 to increase if the subunits are made larger (r_3). Variations of r_1, r_2, r_3 (fig. 7) and ψ (fig. 6) effect the superposition pattern close to the tube axis, whereas departures from mirror symmetry caused by differential flattening (fig. 9) and staining (fig. 10) are most prominent near the tube edges. It was helpful, therefore, to initiate refinement of the differential staining and flattening parameters by comparing features at the edges showing departures from mirror symmetry with the corresponding areas in the experimental image. Parameters were refined by trial and error until further changes failed to significantly improve the fit of model and experimental data. To a resolution of 3.3 nm the model built with symmetric pentamers of spherical sub-

units provides a close approximation to the hexamer tube structure revealed by negative stain.

7. Conclusion

The fit obtained with the observed polyoma "hexamer" tube image shows that a pentamer model built of circular subunits provides a good approximation to the projected image of the capsomere viewed along its axis. On the diffraction pattern of the image, however, there are some clear spots at spacings beyond 1/3 nm spacing that are not present in the diffraction pattern of the model. This implies that there is substructure in the capsomere that cannot be represented by the circular subunit model. Attempts to construct more elaborate models to fit the data may not be rewarding. The diffraction data from the model can, however, be used as a constraint to refine the image data by procedures analogous to those used in low-resolution refinement of crystallographic data [18]. Such an approach should extract the clearest representation of the capsomere substructure available from the electron microscope image.

Model-based refinement methods in electron image analysis may provide a way to separate high resolution images of overlapped lattices in which interference effects would confuse the details that could be resolved in the individual layers using filtering or correlation methods (fig. 14). The results reported here demonstrate distinctive advantages of image modeling methods in defining the large-scale, helical symmetry of flattened tube structures as well as identifying non-crystallographic symmetry within the small-scale repeating unit of the helical surface lattice. Furthermore, image modeling provides a critical way to account for differences in the images of overlapped layers that are due to differential distortion and staining.

Significant details of the pentameric capsomere substructure and bonding relations have been resolved by image modeling applied to the selected polyoma "hexamer" tube described here. These features correlate well with the morphology and packing arrangement of the capsomeres revealed by the 22.5 Å resolution electron density map derived from the X-ray diffraction data [9]. Sys-
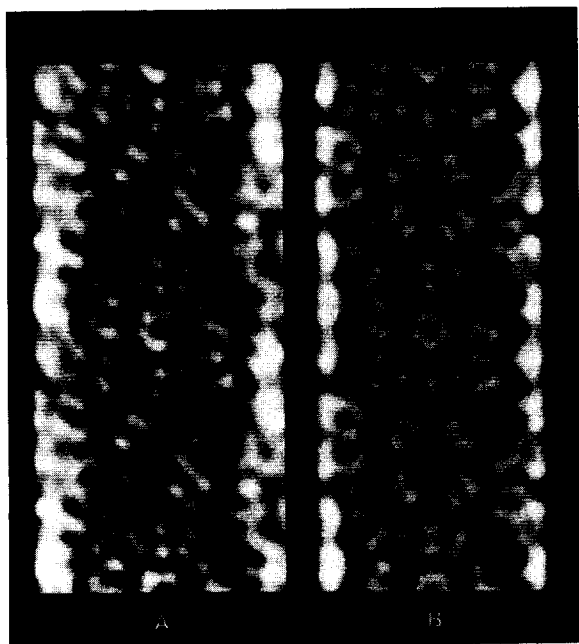

Fig. 11. Comparison of the averaged experimental image (A) with a model simulation (B). Parameters in the model are the same as those in fig. 9D except that the relative contrast between near and far halves is 1.25.

tematic application of the image modeling methods to micrographs of a variety of polyoma virus tube structures will provide an objective way to define the conserved and variable bonding interac-

tions of the pentameric capsomeres that lead to the formation of a range of polymorphic assemblies in which identical subunits are non-equivalently related.
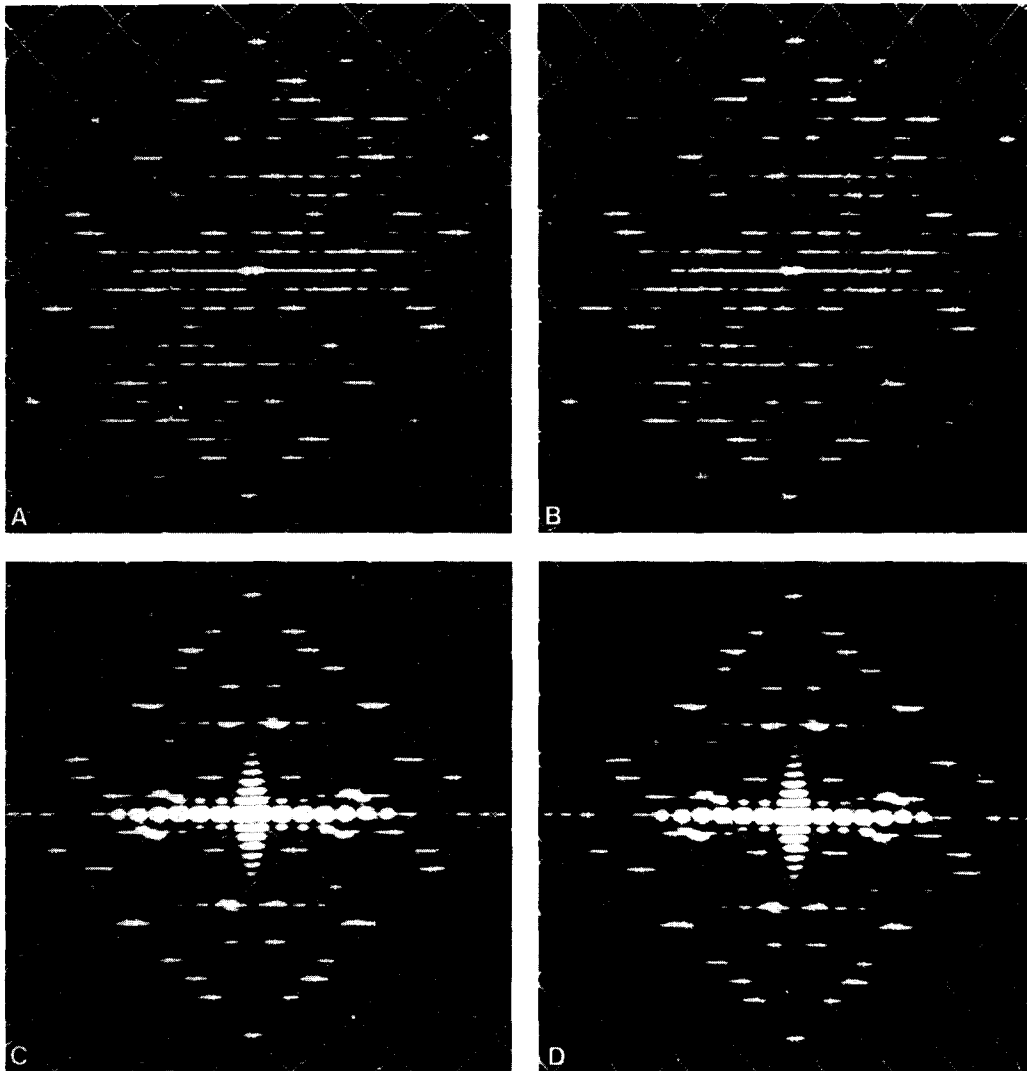

Fig. 12. Comparison of the computed diffraction patterns from the filtered experimental image (A, B; same as fig. 1E) and from the model shown in fig. 11B (C, D). (A) and (C) show the indexed reciprocal lattices from the near sides of the experimental and model images, and (B) and (D) show the far-side indexing. The near and far lattices are not mirror-symmetric due to the unequal distortions in the two halves of the tube specimen; this differential shrinkage is actually simulated in the diffraction patterns of the model. In the example shown, the flattening on the two halves fortuitously leads to overlaps of some reciprocal lattice points from the two sides on the 6th and 7th layer lines (the two lattices necessarily overlap at the meridional position on the 12th layer line for a helical structure with $\sigma = 12/5$ screw symmetry).
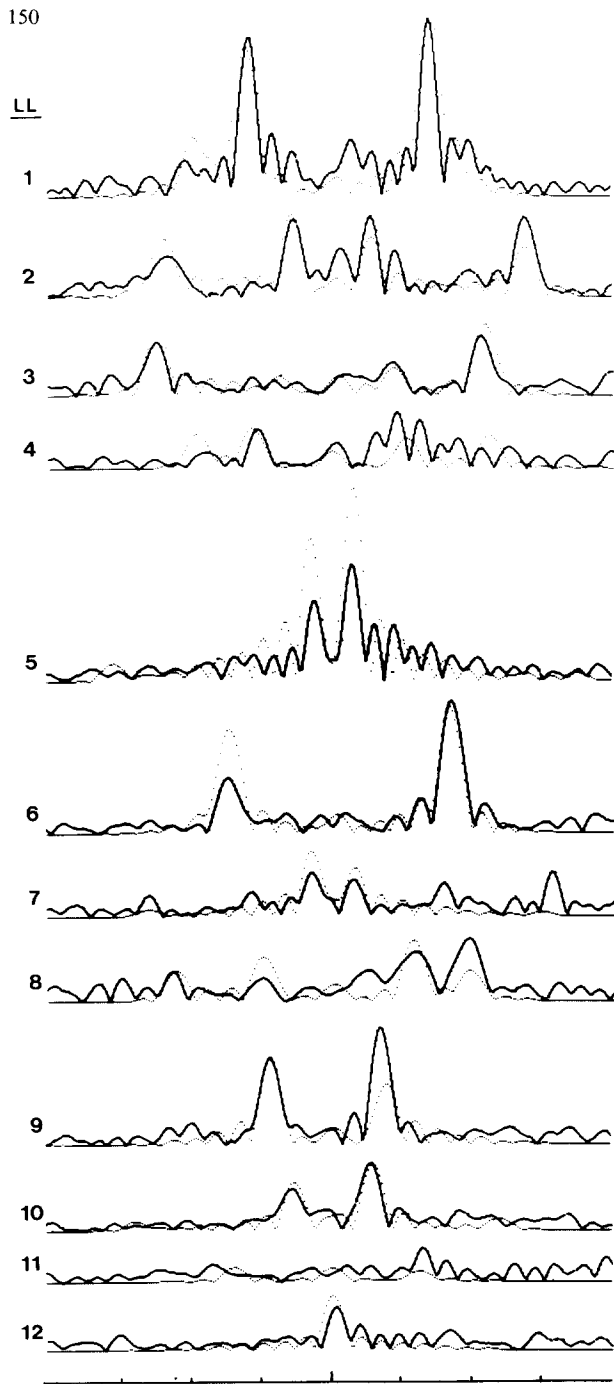
LL

Fig. 13. Comparison of the amplitudes along non-equatorial layer lines for the experimental (solid) and model (dotted) data. The scale factor between data sets is constant for all layer lines shown. The two sets of data differ most on the equator (not shown) and layer line 5 due to the large contrast difference between the edges of the model and its background compared with the stained specimen supported on a carbon substrate. Large differences near the ends of the layer lines (i.e. at higher resolution) reflect the higher noise in the experimental data. The close correspondence of the strong peaks comparing the
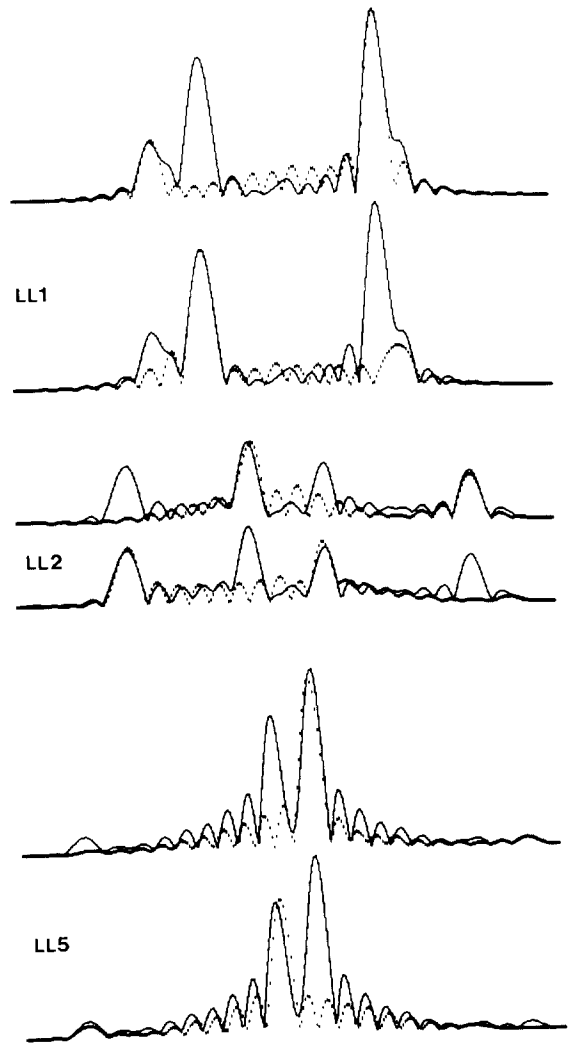

Fig. 14. Examples of interference in the diffraction from the two sides of the model. The solid curves plot the diffraction from the two-sided model for layer lines 1, 2 and 5. (These curves are identical to the corresponding dotted curves in fig. 13.) In each pair of layer line plots, the contribution of the near and far sides alone is shown by the upper and lower dotted curve respectively. The measured amplitude is not simply the sum of the near and far sides calculated separately. The interference effects, for example, lead to cancellation of subsidiary fringes at the center of layer line 1 and to enhancement of the outer fringes on layer line 5. Furthermore, peaks corresponding to lattice points overlap on layer line 1 and are shifted and modulated by overlapping subsidiary fringes on layer lines 2 and 5. These examples illustrate that interference effects make it difficult to separate the diffraction from the two sides by straightforward filtering procedures. More elaborate deconvolution procedures could be used to recover the undistorted diffraction from each side.

experimental and model transforms provides an objective measure of how well the model built with dimers of pentamers represents the structure of this "hexamer" tube.

Acknowledgements

References

[1] A. Klug and J.T. Finch, J. Mol. Biol. 11 (1965) 403.
[2] J.T. Finch and A. Klug, J. Mol. Biol. 13 (1965) 1.
[3] M.G. Williams, A.F. Howatson and J.D. Almeida, Nature 189 (1961) 895.
[4] P. Wildy, M.G.P. Stoker, I.A. Macpherson and R.W. Horne, Virology 11 (1960) 444.
[5] A.F. Howatson and L.V. Crawford, Virology 21 (1963) 1.
[6] D.L.D. Caspar, J. Mol. Biol. 15 (1966) 365.
[7] A. Klug and J.T. Finch, J. Mol. Biol. 31 (1968) 1.
[8] N.A. Kiselev and A. Klug, J. Mol. Biol. 40 (1969) 155.
[9] I. Rayment, T.S. Baker, D.L.D. Caspar and W.T. Murakami, Nature 295 (1982) 110.
[10] J.T. Finch, J. Gen. Virol. 24 (1974) 359.
[11] D.L.D. Caspar and A. Klug, in: Proc. 27th Cold Spring Harbor Symp. on Quantum Biology, 1962, p. 1.
[12] T.S. Baker, D.L.D. Caspar and W.T. Murakami, Nature 303 (1983) 446.
[13] A. Klug, in: Symmetry and Function of Biological Systems at the Macromolecular Level, Eds. A. Engstrom and B. Strandberg (Wiley, New York, 1969) p. 313.
[14] A. Klug and D.J. DeRosier, Nature 212 (1966) 29.
[15] H.P. Erickson, W.A. Voter and K. Leonard, Methods Enzymol. 49 (1978) 39.
[16] T.S. Baker and L.A. Amos, J. Mol. Biol. 123 (1978) 89.
[17] U. Aebi, P.R. Smith, J. Dubochet, C. Henry and E. Kellenberger, J. Supramol. Struct. 1 (1973) 498.
[18] I. Rayment, Acta Cryst. A39 (1983), 102.